A NUMERICAL STUDY OF NOCTURNAL WAVELIKE MOTION IN FORESTS

XINZHANG HU[1], XUHUI LEE[1,⋆], DAVID E. STEVENS[2] and RONALD B. SMITH[3]
[1]*School of Forestry and Environmental Studies, Yale University, Connecticut, U.S.A.;* [2]*Atmospheric Science Division, Lawrence Livermore National Laboratory, Livermore, California, U.S.A.;*
[3]*Department of Geology and Geophysics, Yale University, Connecticut, U.S.A.*

(Received in final form 26 June 2001)

Abstract. In this paper, we use a two-dimensional eddy-resolved model to investigate the instability of a parallel shear flow in a stably stratified boundary layer whose lower domain is occupied by a canopy. The results support our contention that wave motion in the canopy is initiated by shear in an air layer near the treetops. Significant modification by the wave motion of the mean velocity and temperature fields is found even before the wave reaches saturation. The wave fluxes of momentum and heat are not constant with height. Downwind tilting braids are found at the finite amplitude stage of the wave growth and could persist after wave breaking; these downwind tilting structures are believed to be the same as the temperature microfronts reported in the literature. We also present an analysis of the velocity and temperature fields of an observed wave event in the time-height domain and show that the simulation has captured the broad features of the observation.

Keywords: Canopy turbulence, Forest, Numerical model, Shear instability.

1. Introduction

Coherent structures of the turbulence in plant canopies are a subject of numerous micrometeorological studies (Raupach et al., 1996; Finnigan, 2000). In unstable air, these structures are manifest in the form of repetitive temperature ramps (gradual rise in temperature followed by a sharp drop), sweeps, which bring fast moving air downward ($u' > 0$, $w' < 0$), and ejections, which displace slow moving air upward ($u' < 0$, $w' > 0$). Here u and w are the longitudinal and vertical velocities, respectively, and primes denote a departure from the mean. At night when air is stably stratified, the time series of velocities, temperature and other scalars often exhibit a high degree of periodicity. The periodic patterns at times may look like inverse ramps, sinusoidal waves, or square waves. One way to distinguish these coherent motions is to examine the phase relation between w and other quantities. For example, w' and u' are roughly 180° out of phase during a sweep/ejection event in unstable conditions and w' and T' are nearly in-phase, resulting in significant transports of momentum and heat in the air layer near the canopy. On the other hand, wavelike motions often show a 90° phase relation between w' and u' and are not as effective as the sweeps/ejections in transporting momentum (Figure 1).

⋆ Author for correspondence: E-mail: xuhui.lee@yale.edu

Boundary-Layer Meteorology **102:** 199–223, 2002.

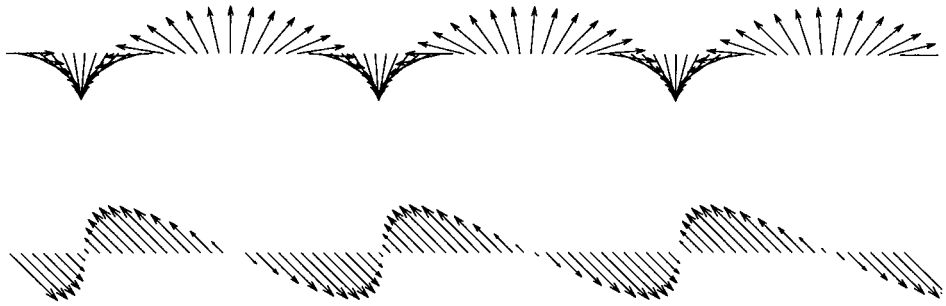

Figure 1. Vector plot of fluctuating velocities showing two idealized phase relations. Top: evanescent wave (u' leading w' by $\pi/2$); bottom: sweep/ejection (u' leading w' by π).

Wavelike motions are a common form of air motion in forests (Fitzjarrald and Moore, 1990; Lee and Barr, 1998). In an earlier study (Lee, 1997), we used a linear model to show that the mean atmospheric state permits an unstable mode that shares common features with the Kelvin–Helmholtz (KH) instability. The linear analysis however suffers from several drawbacks. First, it assumes a constant background flow. In reality, however, the background flow is always evolving due to wave, canopy and mean flow interactions and change in external forcing. Second, linear models apply to small-amplitude, sinusoidal waves. In field experiments wavelike motions are identified only after they have grown to finite amplitudes. They seldom resemble pure sinusoidal waves. Third, the measured wind and scalar fields often show evidence of turbulent mixing, which is a highly nonlinear phenomenon. Numerical simulations are a suitable next step beyond the linear framework to generate further new insights into the dynamics of this motion type.

In this paper, we present the results of a two-dimensional (2D) numerical study of instability of a parallel shear flow in a stably stratified boundary layer whose lower domain is occupied by a canopy. Specifically, we are interested in the time evolution of the wave, wave-introduced mixing and modification of the mean fields, and modification of the classical KH instability by plant elements. We also wish to compare the spatial structures seen in the model domain with those captured by the time-height plots of velocity and temperature time series from a field observation.

The justification for a 2D simulation (instead of a three-dimensional LES) is that the primary KH wave is 2D and is quite persistent in the initial stage of growth. In the linear framework, a 2D treatment of the KH wave is justified according to Squires theorem (Drazin and Reid, 1981). Only after the primary wave has reached a saturation stage do 3D features appear in the flow (Werne and Fritts, 1999). Even then the quasi 2D, large-scale structures still persist in the presence of small-scale 3D fluctuations. These structures are believed to be the vestige of the primary instability in the early stage of flow transition from the laminar to turbulent state (Klaassen and Peltier, 1985). We acknowledge that models of this

type are not new. The 2D studies by Patnaik et al. (1976) and Peltier et al. (1978) substantiated the broad features, such as phase speed and growth rate of the primary mode, predicted by linear analysis. These studies also discussed the time evolution of the wave structure. Schilling and Janssen (1992) embedded in the flow field simulated by a 2D model a Lagrangian dispersion scheme to explain mixing of pollutants caused by the KH instability in the stratosphere. Sykes and Lewellen (1982) used a second-order closure scheme in their 2D model to parameterize the 3D turbulence within the KH billows. In this study we will use a simple 1.5 order closure scheme to parameterize the subgrid-scale turbulence. Since the large-scale structures, the main focus of our study, are essentially determined by the initial and boundary conditions, and to a lesser extent by canopy drag on the air motion, the quality of the turbulence closure model is not critical.

2. Numerical Model

2.1. Basic equations

Our 2D eddy-resolved model explicitly solves the motion with scales larger than the grid size and the effects of the subgrid-scale motions are modelled. The formulation is similar to that of the large-eddy simulation of canopy flow (e.g., Shaw and Shumman, 1992), except that the computation is performed in the $x-z$ plane. The grid-cell averaged governing equations are:

$$\frac{\partial \bar{u}_i}{\partial t} + \frac{\partial}{\partial x_j}\left(\bar{u}_j \bar{u}_i\right) = -\frac{1}{\rho_0}\frac{\partial p'}{\partial x_j} + g\frac{\theta'}{\bar{\theta}_0}\delta_{i3} + \frac{\partial \tau_{ij}}{\partial x_j} + F_i, \tag{1}$$

$$\frac{\partial \bar{\theta}}{\partial t} + \frac{\partial}{\partial x_j}\left(\bar{u}_j \bar{\theta}\right) = \frac{\partial}{\partial x_j}\left(\overline{u_j' \theta'}\right), \tag{2}$$

$$\frac{\partial \bar{u}_i}{\partial x_i} = 0, \tag{3}$$

where u_i ($i = 1, 3$) is the velocity component in the x_i direction, θ is potential temperature, p is pressure, ρ is air density, g is gravitational acceleration, and p' and θ' are deviations from the adiabatic background pressure and potential temperature, respectively. Overbars denote grid-cell averaging. Canopy drag, F_i, is modelled, following Shaw and Schumann (1992), as,

$$F_i = -c_d a V \bar{u}_i, \tag{4}$$

where V is instant scalar total velocity, a is leaf area density, and c_d is a drag coefficient (= 0.15; Shaw et al., 1988). Air-plant heat exchange is omitted from Equation 2 for computational convenience. A sensitivity analysis with our linear

model suggests that the omission may lead to a slight (5–10%) increase in the growth rate but does not affect phase speed or wavelength of the fastest growing mode.

The subgrid-scale momentum and heat fluxes are written as

$$\tau_{ij} = \bar{u}_i \bar{u}_j - \overline{u_i u_j} = K_m \left(\frac{\partial \bar{u}_i}{\partial x_j} + \frac{\partial \bar{u}_j}{\partial x_i} \right) - \frac{2}{\delta_{kk}} E \delta_{ij}, \tag{5}$$

$$\overline{u_j}\overline{\theta} - \overline{u_j \theta} = K_h \frac{\partial \overline{\theta}}{\partial x_j}, \tag{6}$$

where K_m and K_h are the subgrid eddy viscosities of momentum and heat, respectively, and $E = \overline{u_i'^2}/2$ is the subgrid-scale turbulent kinetic energy. The eddy viscosity is obtained from the Prandtl–Kolmogorov relation,

$$K_m = K_h = c_m l E^{1/2}, \tag{7}$$

where c_m is an empirical constant (= 0.15), and l is the characteristic length scale which is related to the horizontal and vertical grid sizes Δx and Δz by $l = (\Delta x \Delta z)^{1/2}$. The turbulent kinetic energy is determined by the following prognostic equation

$$\begin{aligned} \frac{\partial E}{\partial t} + \frac{\partial (\bar{u}_j E)}{\partial x_j} &= \frac{\partial}{\partial x_j}(K_m \frac{\partial E}{\partial x_j}) + K_m (\frac{\partial \bar{u}_i}{\partial x_j} + \frac{\partial \bar{u}_j}{\partial x_i}) \frac{\partial \bar{u}_i}{\partial x_j} \\ &\quad - K_h \frac{g}{\theta_0} \frac{\partial \theta'}{\partial x_j} \delta_{j3} - c_\epsilon \frac{E^{3/2}}{l} + c_d a V^3, \end{aligned} \tag{8}$$

with the empirical constant $c_\epsilon = 0.93$.

2.2. NUMERICAL METHODS

The MATLAB flow solver for solving the model equations is developed by Stevens et al. (2000). The same algorithm was used to study the entrainment process in a stratocumulus marine boundary layer (Stevens et al., 2000). The numerical scheme is based on the algorithm developed by Almgren et al. (1996). This projection method is a fractional step scheme, and first solves the advection- diffusion equations to predict intermediate velocities, and then projects these velocities onto the space of approximately divergence-free vector fields. A second-order upwind method is adopted to discretize the nonlinear advection terms, which avoids any cell Reynolds number stability restriction for high Reynolds flow. Compared with standard upwind differencing methods, the scheme couples the spatial and temporal discretization to attain a second-order accuracy in both space and time. It leads to a robust higher order discretization with excellent phase-error properties. Unlike the widely-used staggering grid layout, all primary variables to be computed

are located in the centres of the grid cells so that no interpolation is needed to compute the model statistics, such as momentum flux and heat flux. The time-step constraint is the common Courant–Friderich–Levy condition

$$\max\left(\frac{|u|\,\Delta t}{\Delta x}, \frac{|w|\,\Delta t}{\Delta z}\right) \leq 1.$$

2.3. Initial and boundary conditions

The lateral boundaries are periodical, which is appropriate for this simulation study. The length of the computation domain is set to one wavelength of the fastest growing mode predicted by the linear wave model (Lee, 1997). The domain height is $6h$, where h is canopy height. The upper and lower boundaries are treated as rigid walls and zero-flux conditions are implemented. The upper boundary is sufficiently far away from the maximum shear, and hence has a negligible effect on the flow development.

The same profiles in the linear canopy wave model (Lee, 1997) are used to initiate our simulations. A Gaussian distribution describes the leaf area density

$$a(z) = \frac{Lh}{0.125\sqrt{2\pi}} \exp\left[-(z/h - 0.65)^2 / \left(2 \times 0.125^2\right)\right] \tag{9}$$

where z is height and L is leaf area index. The initial mean wind speed is given by

$$u = \begin{cases} u_h \exp\left[\alpha_2 (z/h - 1)\right] & z \leq h, \\ u_h \left\{\alpha_1 \tanh\left[(\alpha_2/\alpha_1)(z/h - 1)\right] + 1\right\} & z > h, \end{cases} \tag{10}$$

where $u_h = 1\ \mathrm{m\,s^{-1}}$ is the wind speed at $z = h$, α_1 (= 3) and α_2 (= 2.85) are empirical constants. The temperature profile is set up to make the Brunt–Väisälä frequency (N) profile assume the following form

$$N^2 = 0.003\left\{(1 - \gamma_1)\exp\left[-\gamma_2 (z/h - 1)\right] + \gamma_1\right\}, \tag{11}$$

where $\gamma_1 = 0.2$ and $\gamma_2 = 2$.

The parameter values used in the simulation are listed in Table I. The minimum Richardson number is located at $z/h = 1.38$ with a value of 0.112, smaller than the critical value of 1/4. All simulations are initiated with small-amplitude white noise added to the initial potential temperature field. Other variables adjust themselves gradually to the perturbation. At about 200 s after the initiation, the flow field locks into the fastest growing mode. The initial perturbation is sufficiently small so that it does not influence the flow structure at the finite-amplitude stage. Previous studies (e.g., Peltier et al., 1978; Sykes and Lewellen, 1982) have demonstrated the insensitivity of the result to the exact form of the initial perturbation.

TABLE I
Parameters used in the numerical simulations.

Parameter	Definition	Value
Δx	Horizontal grid size	3.28 m
Δz	Vertical grid size	1.88 m
h	Tree height	20 m
L	Leaf area index	4
u_h	Wind speed at treetops	1 m s^{-1}
λ	Wavelength of the fastest growing mode	210 m
L_x	Length of computation domain	λ
H	Height of the computation domain	$6h$

3. Life History of an Observed Wave Event

In this section, we present an analysis of the velocity and scalar fields of an observed wave event in the time-height domain following Gao et al. (1989) and Bergström and Hogström (1989). Since field observations in a 2D spatial domain are not feasible, the features captured by the time-height plots are helpful for us to judge the validity of the model simulations.

3.1. DATA

The data were collected during the 1994 BOREAS (Boreal Ecosystem Atmosphere Studies) field campaign (Lee et al., 1997). The forest was 21 m tall, with a dense 2-m tall understory. At the time of the observation, the overstory and understory leaf area indices were 1.8 and 3.2, respectively. There were three sonic anemometers mounted at z = 5.5, 27.7 and 39.1 m. Air temperature fluctuations were monitored at 12 levels (z = 2.2, 4.1, 6.4, 9.5, 12.6, 15.7, 18.8, 21.9, 25.0, 27.7, 31.4, 39.1 m) with fine wire thermocouples.

The data used in this study, from 0145 to 0300 local standard time (LST), July 13, cover the complete life history of a wave event, from its initiation to breaking. A portion of the data was analyzed by Lee et al. (1997). Hu (2001) presented a full account of the time evolution of the temperature field and the interactions between the wave and external forcing (cloudiness, mean wind) on the night of July 12–13.

3.2. FLOW AND SCALAR FIELDS IN THE TIME-HEIGHT DOMAIN

A sequence of 5-min temperature contour/velocity vector plots are presented in Figures 3–4, and water vapour and CO_2 time series for the same period are given in Figsures 5–6. The 5-min mean wind speed at $z = 1.9h$ was 1.8 m s^{-1} at

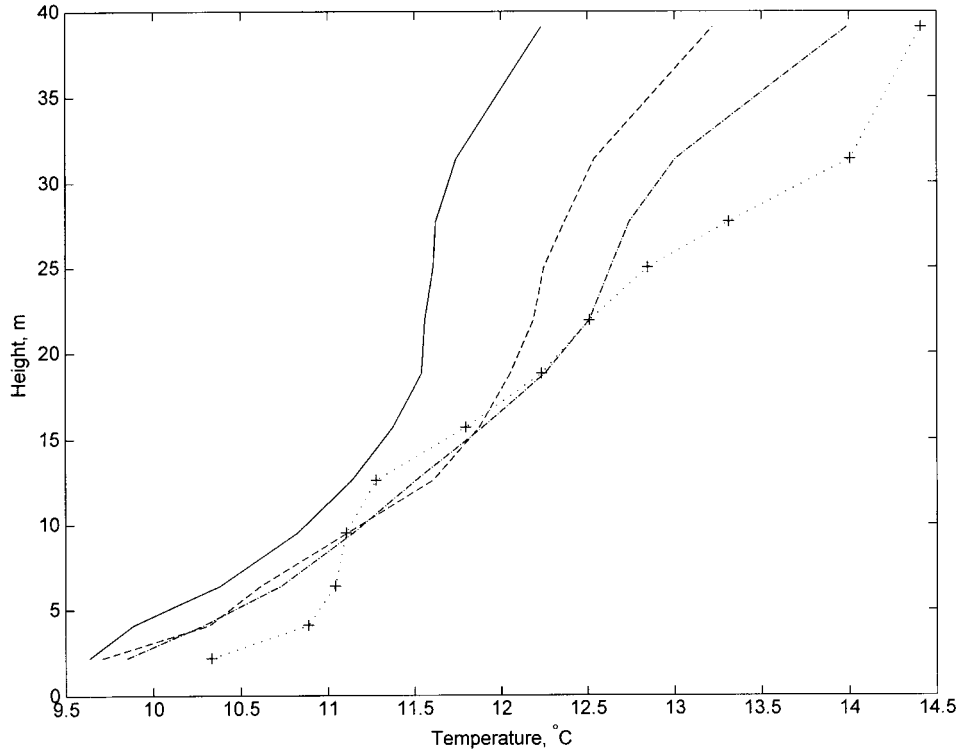

Figure 2. Profile of 5-min mean temperature observed in a boreal forest on July 13, 1994: dotted line with crosses, 0145-0150; dash-dot line, 0205-0210; dashed line 0225-0230; solid line, 0255-0300 LST.

0145 LST and increased steadily to 2.5 m s^{-1} at 0300 LST. Net radiation over the forest was -75 W m^2. The 5-min mean temperature and its vertical gradient decreased steadily with time due to radiative cooling and wave mixing, respectively (Figure 2).

3.2.1. *Wave Initiation*

In the wave initiation stage (Figure 3 top panel), temperature fluctuations were found mainly in the air layer $1h - 1.5h$. Although wind fluctuations at $z = 1.9h$ were small, distinctive periodic patterns were clearly visible. In comparison, wind fluctuations at $z = 1.3h$ were larger and less organized. The remarkably constant concentrations of water vapour and CO_2 at $z = 1.9h$ indicate that there was little vertical displacement of air parcels at this height or that the sensors were located in a previously well-mixed layer (Figure 5 top panel). From these features we may infer that the source of disturbance was located near the treetops rather than in the upper boundary layer beyond the tower height.

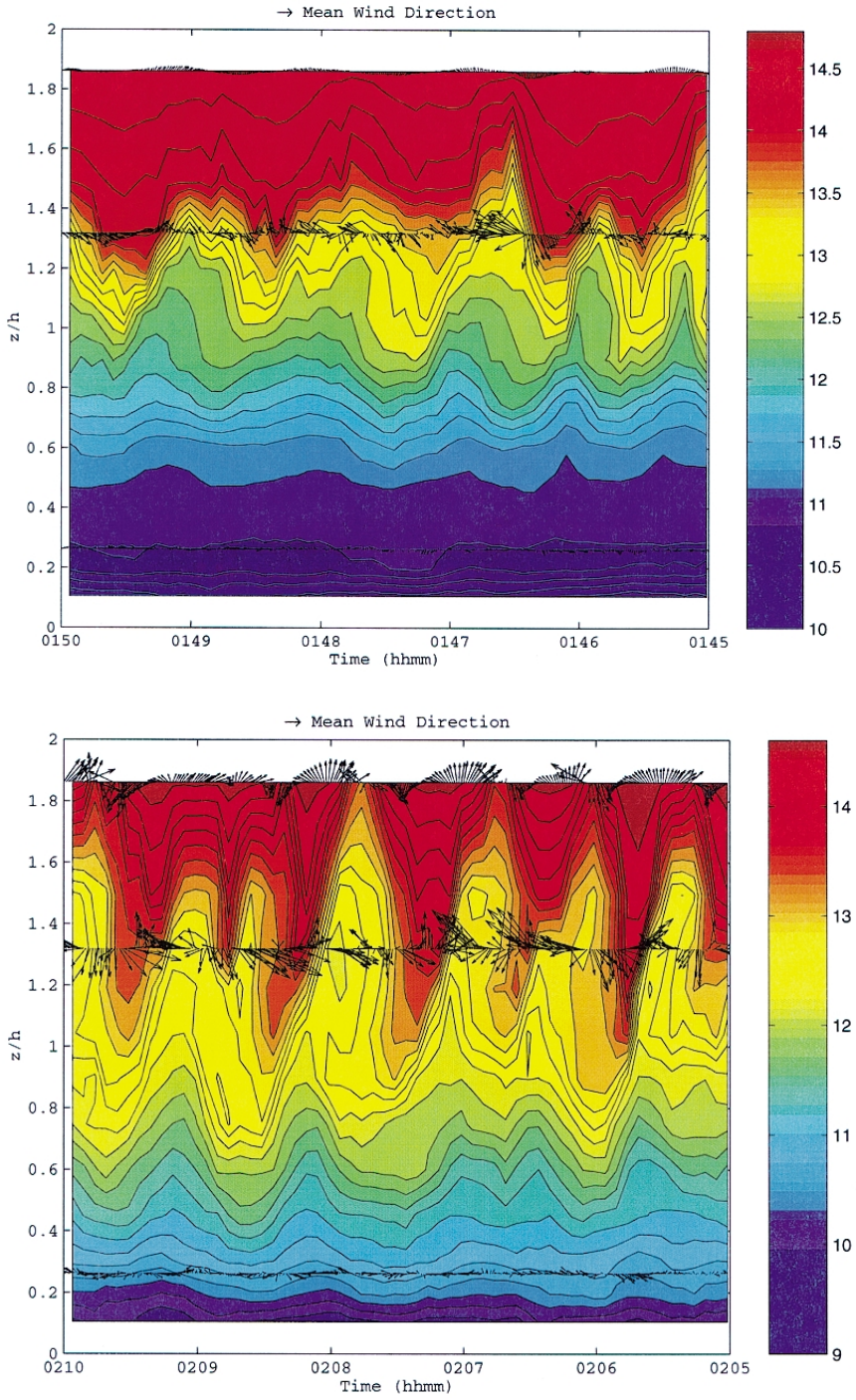

Figure 3. Observed velocity fluctuations superposed on temperature contours at 0.2 K intervals. Top: Wave initiation (maximum wind fluctuation of 0.79 m s^{-1}); bottom: Wave growth (maximum wind fluctuation of 1.01 m s^{-1}).

3.2.2. *Wave Growth*

By 0205 LST, the wave had gained moderate strength (Figure 3 bottom panel). The top most sonic anemometer was located just above the upper limit of the wave core, away from the maximum shear. The wind fluctuation pattern is quite similar to the evanescent wave shown in Figure 1, indicating that w' at $z/h = 1.9$ was approximately in quadrature with u', that is, u' leading w' by $\pi/2$. The wave resulted in little momentum transport despite the relatively large velocity fluctuations. Similarly, w' was also in quadrature with the temperature fluctuations, resulting in little sensible heat flux. The fluctuations in water vapour and CO_2 concentrations were closely associated with the strength of the wave activity (Figure 5 bottom panel). The flat baselines of CO_2 and H_2O were periodically interrupted by spikes that were a result of the wave motion of sufficiently large magnitude bringing air of high CO_2 and low humidity to the sensor height, a pattern consistent with our contention that the wave motion was initiated near the treetops. [The 180° phase between humidity and CO_2 suggests a downward flux of water vapour (dew formation).]

The wave structure was tilted in the downwind direction, a common feature of billow waves (Delisi and Corcos, 1973). Near the centre of the wave cores (e.g., $z = 1.2h$), temperature gradient at the leading edge was more diffusive than at the trailing edge. Hence, a temperature sensor would record a time series characterized by inverse ramps.

The sonic anemometer at $z = 1.3h$ was located in the middle of the wave cores. Once again, wind fluctuations at this height were bigger than those at $z = 1.9h$. Sweep/ejection patterns, similar to the idealized case shown in Figure 1, can be identified. Unlike the daytime coherent structures in which sweeps dominate over ejections, here both motion types were of equal importance in momentum transport. There was a slight positive correlation between w and T over this period, indicating an upward, counter-gradient transport of heat.

3.2.3. *Wave Saturation*

In the next plot (Figure 4 top panel), the wave had reached a stage of maximum intensity, which we label as saturation stage. The wave core extended beyond $z = 1.9h$ on several occasions. A striking feature at $z = 1.9h$ is the alternate quadrature and sweep/ejection phase relations: u' and w' were in quadrature as in Figure 3 when the sensor was outside the wave core and displayed the sweep/ejection pattern when it was within the core. It was these sweeps/ejections that generated downward momentum flux at this height. In other words, momentum flux was only generated over a fraction of a wave cycle. The wind fluctuations were as strong as those at $z = 1.3h$. The square wave pattern in the H_2O and CO_2 time series was also indicative of wave saturation (Figure 6 top panel).

The velocity fluctuations at $z = 1.3h$ show the classical sweep/ejection pattern (Figure 1). The sharp transition from a sweep to an ejection occurred roughly in the middle of the wave core. The highly correlated u' and w' generated a large downward momentum flux. The temperature contours suggest overturning in the

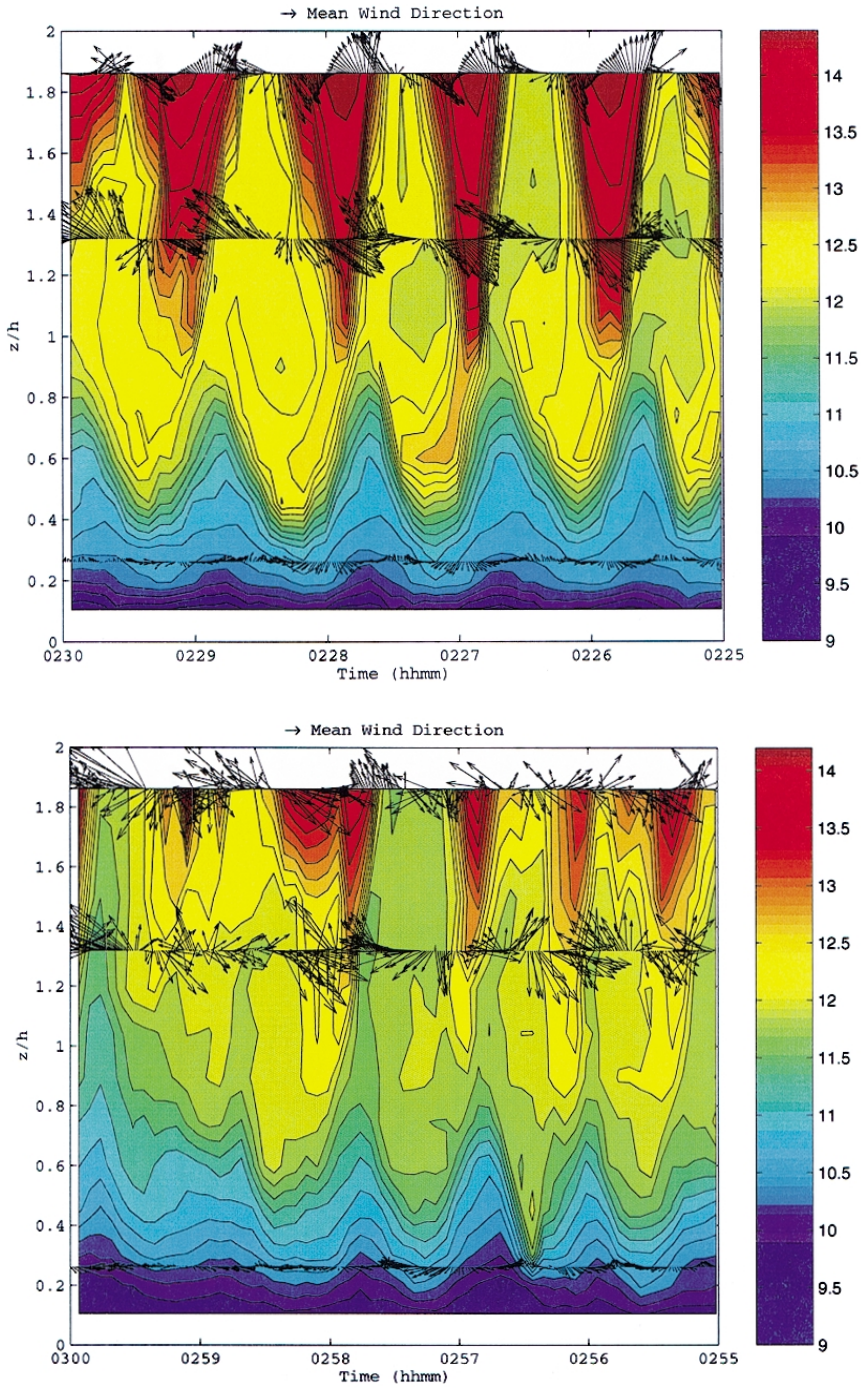

Figure 4. Observed velocity fluctuations superposed on temperature contours at 0.2 K intervals. Top: Wave saturation (maximum wind fluctuation of 1.29 m s^{-1}); bottom: Wave destruction (maximum wind fluctuation of 2.08 m s^{-1}).

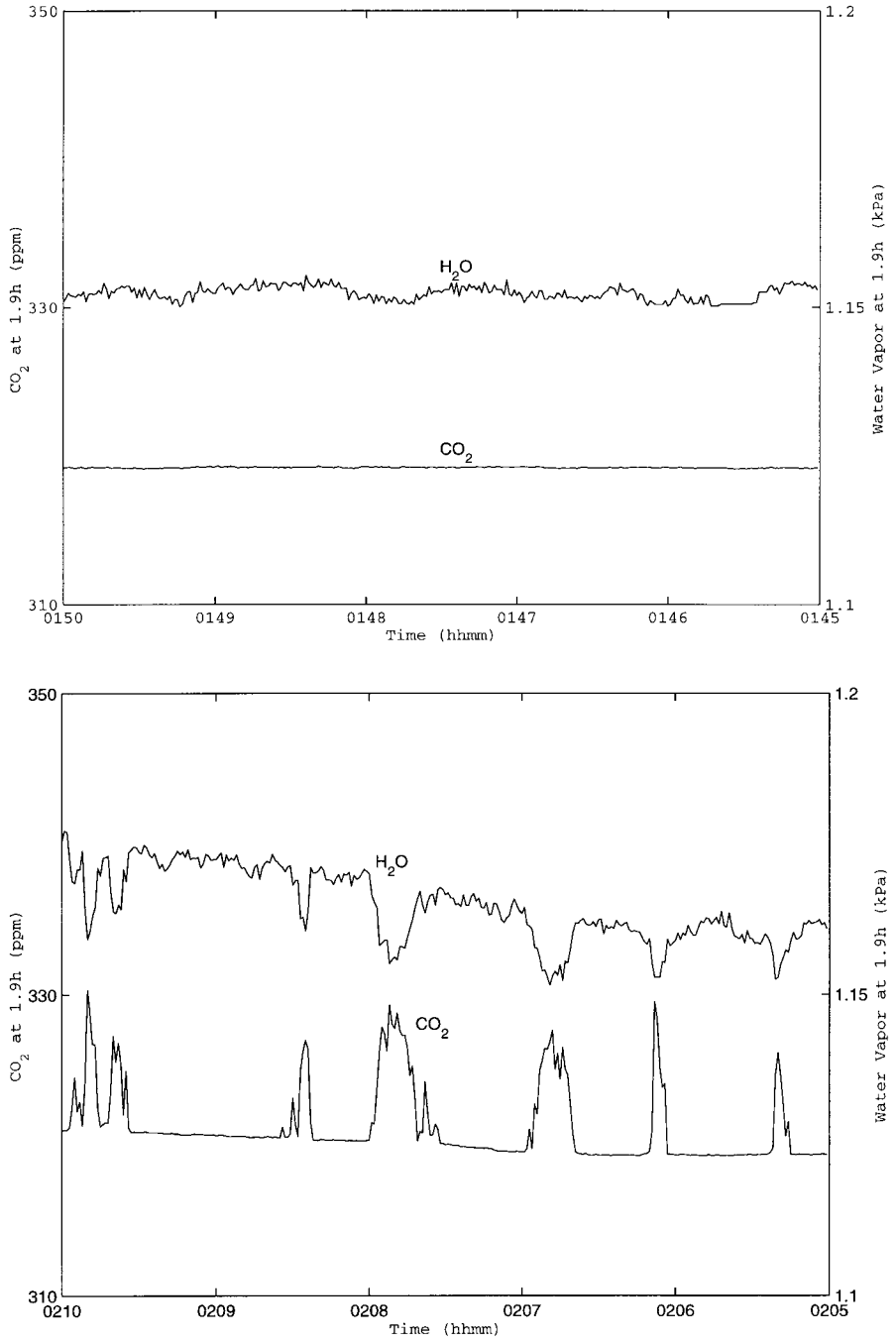

Figure 5. Scalar fluctuations for periods shown in Figure 3.

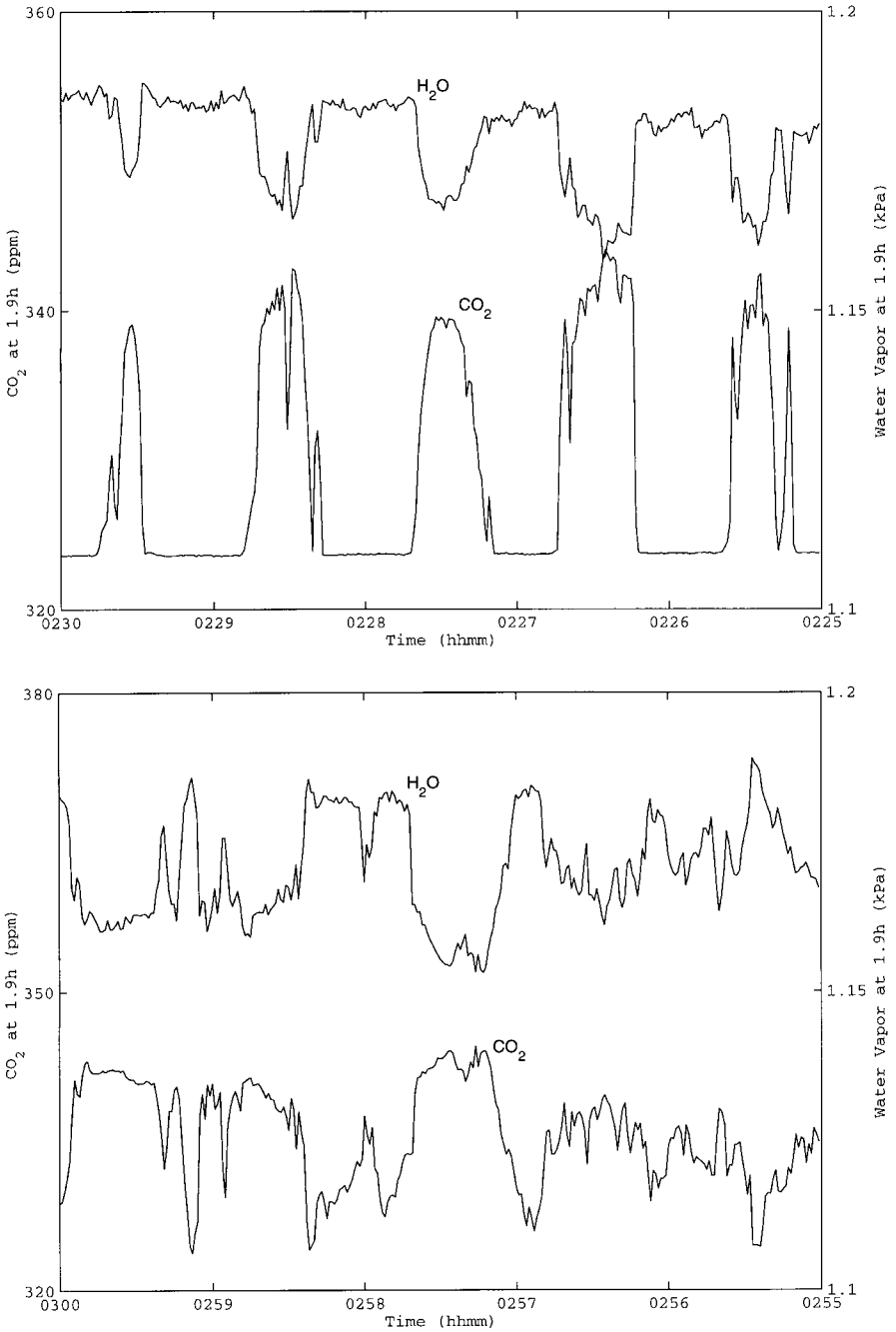

Figure 6. Scalar fluctuations for periods shown in Figure 4.

wave core, that is, some cooler air being brought over the warmer air, and give the impression that the warmer air and cooler air were spinning around each other with a positive spanwise vorticity. Since such overturning structures were statically unstable, turbulence would develop from convective instability, similar to those found in the laboratory experiment (Thorpe, 1987). Indeed, air temperature within the wave core was rather uniform and showed a slight increase with time, which supports the conjecture of turbulent mixing.

The wind at $z = 0.26h$ was fairly strong at this time. The velocity vector plot appears as a mirror image of that shown in Figure 1 (top panel). From this we infer that w' led u' by $\pi/2$. Thus, wave motion within the lower part of the canopy was of the evanescent type.

3.2.4. *Wave Destruction*

In the wave destruction stage (bottom panels of Figures 4 and 6), the steep temperature gradient delineating the wave core began to disappear. Irregularity was evident in the velocity and scalar time series except in the lower canopy layer where the sinusoidal pattern remained. Temperature gradient in the air layer z/h = 1–1.5 was reduced substantially as a result of overturning and wave breaking (Figure 2). This was followed by a one-hour quiescent period and then the initiation of another wave event (Hu, 2001).

4. Results of Numerical Simulations

4.1. Comparison with linear wave theory

Numerical simulations have been carried out for flow with and without the canopy. Because the initial perturbation is sufficiently small in magnitude, the 2D simulations can capture a linear growth stage. The growth rate and phase speed are compared with the linear theory to establish, among other things, confidence of the numerical procedure. A cross-correlation algorithm is used to calculate the phase speed (Appendix A). To estimate the growth rate, we first determine the mean horizontal velocity u in the streamwise direction as

$$\langle u \rangle = \frac{1}{L_x} \int_0^{L_x} u\,(x, z)\ \mathrm{d}x, \tag{12}$$

where L_x is the horizontal domain size. The total perturbation kinetic energy is given by

$$e = \int_0^H \mathrm{d}z \left(\int_0^{L_x} \frac{1}{2} \left[(u - \langle u \rangle)^2 + w^2 \right] \mathrm{d}x \right), \tag{13}$$

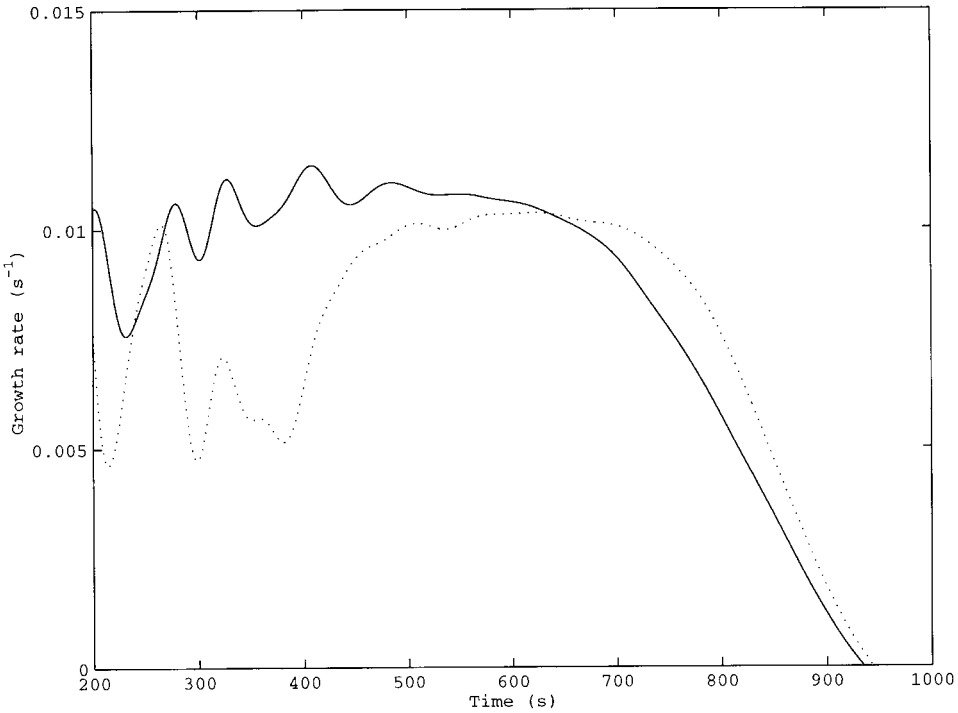

Figure 7. Wave growth rate simulated by the 2D model (solid line, with canopy; dotted line, without canopy).

where H is the height of the model domain. The growth rate of the primary mode is given by

$$\sigma = \frac{1}{2}\frac{\mathrm{d}}{\mathrm{d}t}(\ln e)\,. \tag{14}$$

The result is shown in Figures 7 and 8.

The linear growth stage, characterized with a constant growth rate, is found between 400 s and 700 s, or 4 to 7 linear time constants, noting that a linear time constant is the inverse of the growth rate in the linear stage, for both simulations with and without the canopy drag. The oscillations in the growth rate prior to this are a result of the initialization with white noise, similar to those reported by Peltier et al. (1978). The growth rate without the canopy is 0.010 s^{-1}, identical to the prediction of the linear stability analysis. Inclusion of the canopy drag in the simulation increases the growth rate slightly (0.011 s^{-1}). In comparison, the linear model (Lee, 1997) predicts a growth rate of 0.067 s^{-1} for flow with the canopy effect.

The 2D simulation of flow without the canopy gives a phase speed of about 1.6 m s^{-1} in the linear growth stage, once again in excellent agreement with the linear

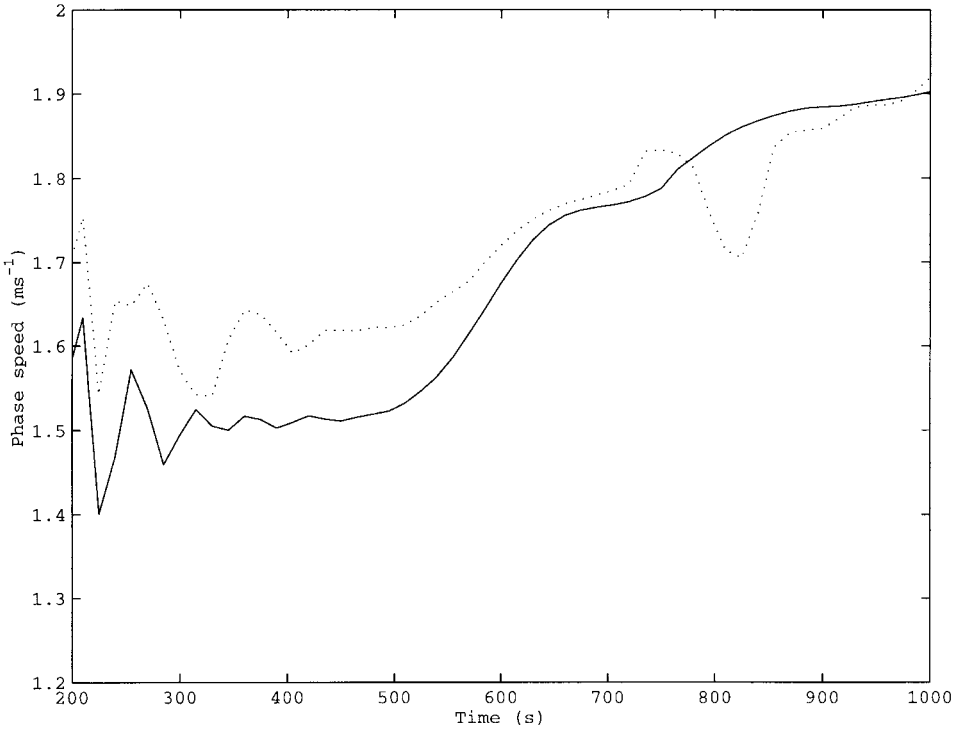

Figure 8. Wave phase speed simulated by the 2D model (solid line, with canopy; dotted line, without canopy).

model prediction (Figure 8). For flow with the canopy, the phase speed is reduced to 1.5 m s^{-1}, 8% lower than the linear model prediction.

The agreement on the linear growth parameters between the 2D simulation and linear stability analysis for flow without the canopy is similar to previous studies on KH instability (Patnaik et al., 1976; Peltier et al., 1978) and is indicative of a good performance of our 2D flow solver. The discrepancy for the simulation with the canopy can be understood in terms of the changing background flow (next sub-section). Once the wave has grown beyond the linear stage, the growth rate decreases to zero within 2–3 linear time constants (Figure 7). The 2D flow structures indicate that the wave becomes saturated in amplitude at $t = 900$ s (Figure 9 below). The phase speed increases steadily to 1.9 m s^{-1} at wave saturation (Figure 8). A saturated canopy wave propagates at an increased speed because the shear layer has been broadened by wave mixing.

4.2. The role of canopy drag in the wave dynamics

Even though the canopy drag represents a momentum sink (Equation (1)) and hence some stabilizing effect on the flow, its overall role is to destabilize the flow through the KH instability. The process can be understood if we start with

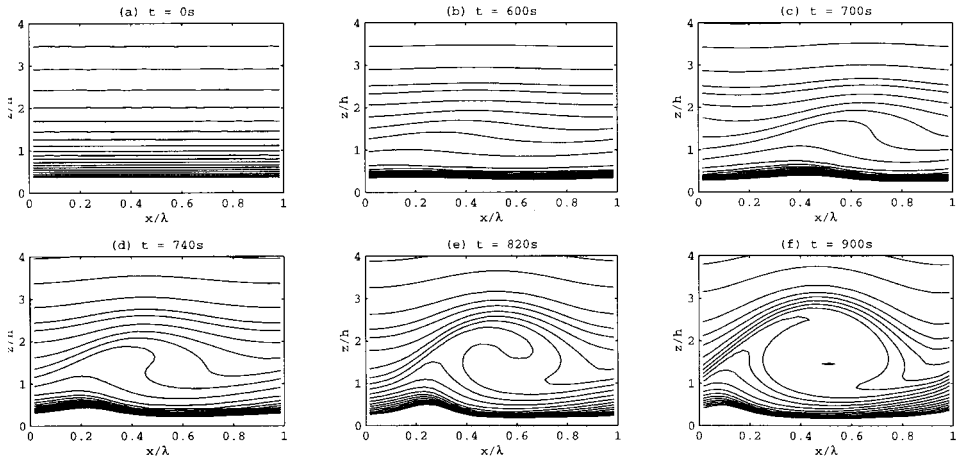

Figure 9. Evolution of the simulated temperature field in the $x - z$ domain. The layer $z < h$ is occupied by a plant canopy. Wind is from left to right. Contour interval is 0.2 K.

a hypothetical quiescent period during which air is stably stratified and wind speed is very low both within and above the canopy. Let us now suppose that a sporadic external forcing, such as the breakdown of a nocturnal low-level jet, speeds up the background flow. Initially, the wind speed is modified only by the canopy drag because the flow is essentially laminar. The time constant for a shear layer to establish can be estimated from

$$F_c = c_d a u^2 = u/2t_c, \tag{15}$$

where $t_c = 2/c_d a u$ is referred to as half time, the time needed for the wind within the canopy to be reduced by a half, and is similar to the concept of distance constant proposed by Finnigan and Brunet (1995). For a 20-m tall forest with a leaf area index of 5 and foliage uniformly distributed with height, an initial wind speed of $u = 2$ m s^{-1}, and a canopy drag coefficient $c_d = 0.15$, the half time is about 10 s. Thus, in a very short time wind shear is established near the treetops. The initial shear layer is thin for lack of turbulence mixing, with a shear that may be strong enough to reduce the Richardson number below the critical value and thus trigger the KH instability. The thin shear layer will limit the initial instability to small scales, but will be broadened by the subsequent mixing. Further instability at a larger scale may be triggered in the broadened shear layer or by merging of previous small-scale waves. It is possible that several such instability cycles may occur before the wave is observable by the eddy covariance instruments.

The effect of the canopy drag on the wave dynamics is captured to some extent by comparing the 2D simulation and the linear analysis. In the linear analysis, the background flow is assumed constant with time. However, in the 2D numerical simulation, because the half time of wind adjustment within the canopy is much shorter than the linear time constant, a significant reduction in the wind in the

canopy layer occurs almost immediately after the simulation is initiated. As a result, the instability grows on a background wind profile whose shear is actually larger than the initial shear given by Equation (10) and thus a larger growth rate is computed. Likewise, because the instability moves at a speed of the mean wind near the canopy top, which is reduced from the initial value, the phase speed is smaller than predicted by the linear analysis. Unfortunately, our 2D model cannot reproduce the small-scale KH waves proceeding the primary mode because the model forces the instability to lock onto a specified wavelength equal to the domain length (Table 1).

4.3. Two-dimensional wave evolution

The simulation is initiated at $t = 0$ s with a small disturbance added to the background temperature field. From a sequence of the simulated temperature contour plots (Fig. 9), we can identify the first three stages of the wave development: wave initiation ($t < 600$ s), wave growth (600–740 s) and wave saturation (820–900 s), each bearing resemblance, at least in a qualitative sense, to the observation described above. The horizontally homogeneous stratification becomes visibly distorted as the waves grow beyond the linear stage ($t = 600$ s). Not surprisingly, the distortion starts in a layer near the treetops where the maximum shear occurs. Further growth of the wave gives rise to two broad features of the classical KH instability (Patnaik et al., 1976; Peltier et al., 1978), the roll-up of the temperature contours in the wave core and crowding of these contours along an inclined band called 'braid'. The braid, located on the downwind side of the wave core, connects the top of one core to the bottom of the next (also Figure 10 below). The horizontal temperature gradient upwind of the core is more diffuse than in the braid. Thus an imaginary temperature sensor at the height of the wave core would record a time series characterized with inverse ramps. Overturning structures similar to the observation (Figure 4 top panel) are found at 820 s. At 900 s, the wave has reached its finite amplitude and become saturated, with a core of uniform temperature due to overturning.

In Figure 10, the wind fluctuation vectors are superposed on the potential temperature field at $t = 800$ s. Three identical frames are patched together to allow a visual comparison with the field observation. The maximum velocity fluctuations are found within the wave core. (The rather large wind fluctuations near the ground are unrealistic since the lower boundary condition in the calculation does not provide a momentum sink.) The simulated vertical velocity above the billow core is in quadrature with the horizontal velocity. This evanescent feature is expected because the mean fields in this air layer (Equations (9)–(11)) satisfy the condition

$$N/(c - \langle u \rangle) < 2\pi/\lambda, \tag{16}$$

where c is phase speed. The wind fluctuations within the billow core display clearly the sweep/ejection pattern, allowing the wave motion to extract kinetic energy from

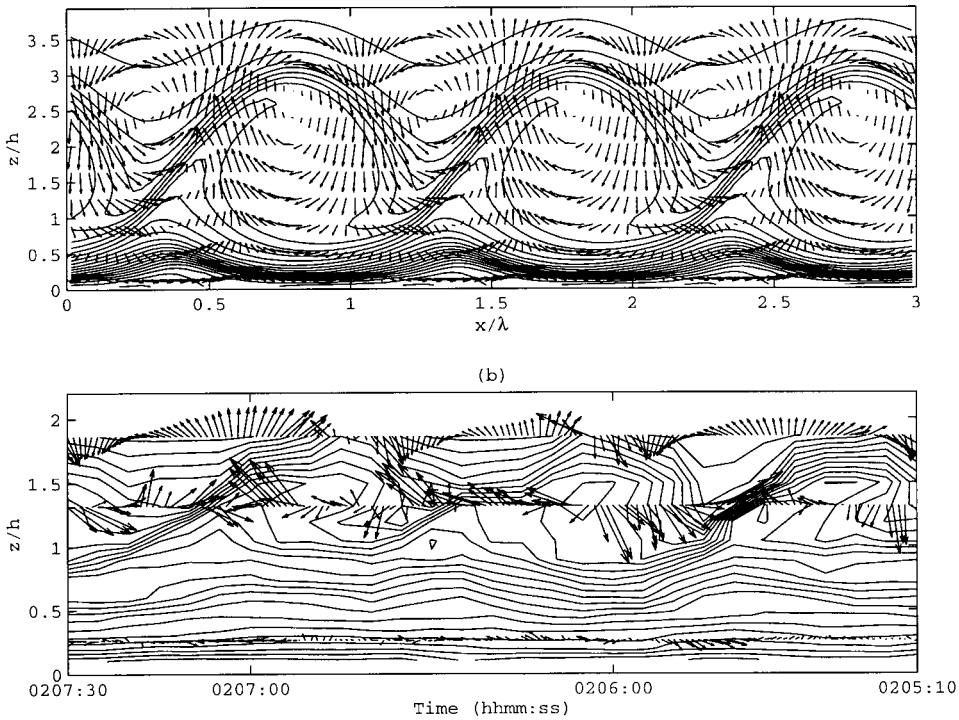

Figure 10. Top: Simulated velocity fluctuation vectors superposed on the temperature contours at t = 800 s in the presence of a canopy (contour interval 0.2K, maximum wind fluctuation 1.01 m s^{-1}). Bottom: Observed velocity/temperature fields (a portion of the data shown in Figure 3 bottom panel).

the mean flow at the maximum shear height and to re-distribute the energy. The height-dependent phase relation is similar to the observation discussed above except that the layer of simulated wave disturbance is much deeper than the observed one.

In a reference frame moving with the mean flow, the classical KH instability is characterized with a closed streamline pattern known as 'cat's eye' (Draizn and Reid, 1981). Here we check the streamlines of the simulated canopy wave. The stream function is defined as

$$\phi = \int (u - c)\, \mathrm{d}z, \tag{17}$$

and a sequence of streamline plots is presented in Figure 11. Closed streamlines are found at t = 520 s at height $z/h = 1.35$, near the height of the minimum Richardson number of the initial velocity and temperature fields. In the moving reference frame, the fluid circulates along the vorticity lines associated with the initial shear. As the wave grows, the centre of the cat's eye moves slightly upward and its major axis turns slightly in the clockwise direction. The pattern is not

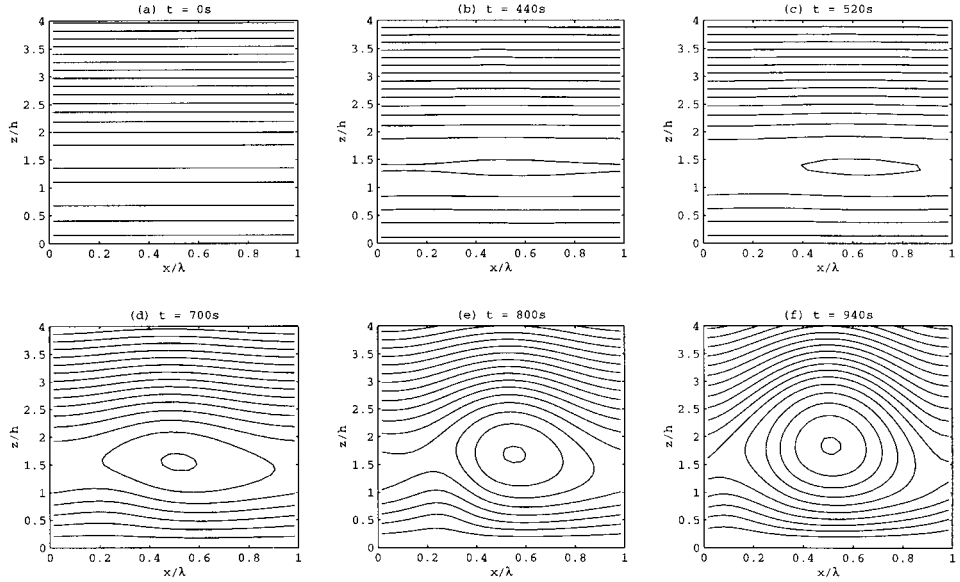

Figure 11. Simulated streamlines at various time steps for flow with a canopy.

symmetrical because of the unsymmetrical wind profile and the effect of canopy drag.

4.4. WAVE INTRODUCED MIXING

The role of the above $u' - w'$ phase relation in momentum transport can be further understood by examining the mean wind profile and a horizontally averaged momentum flux computed as

$$\langle u'w' \rangle = \frac{1}{L_x} \int_0^{L_x} (u - \langle u \rangle)(w - \langle w \rangle)\, \mathrm{d}x, \tag{18}$$

noting that this is a flux from the resolved-scale motion. A constant flux layer does not exist over the canopy (Figure 12); the divergence of the momentum flux above the maximum shear height ($z/h > 1.2$) leads to deceleration there. The momentum flux exhibits a convergence pattern below the maximum shear height, but because the canopy is a momentum sink, the flow does not accelerate. A small secondary wind speed maximum appears near the forest floor at t = 600 s, perhaps related to an open trunk space specified by the leaf area density profile (Equation (9)). Flow reversal occurs near the ground at the wave saturation stage (t = 900 s), at the same time when the momentum flux exhibits a kinky pattern. This suggests some effect of entrainment of fast fluid into the slow-moving lower layer as discussed by Peltier et al. (1978), or else a numerical artifact of the lower zero-flux rigid boundary condition.

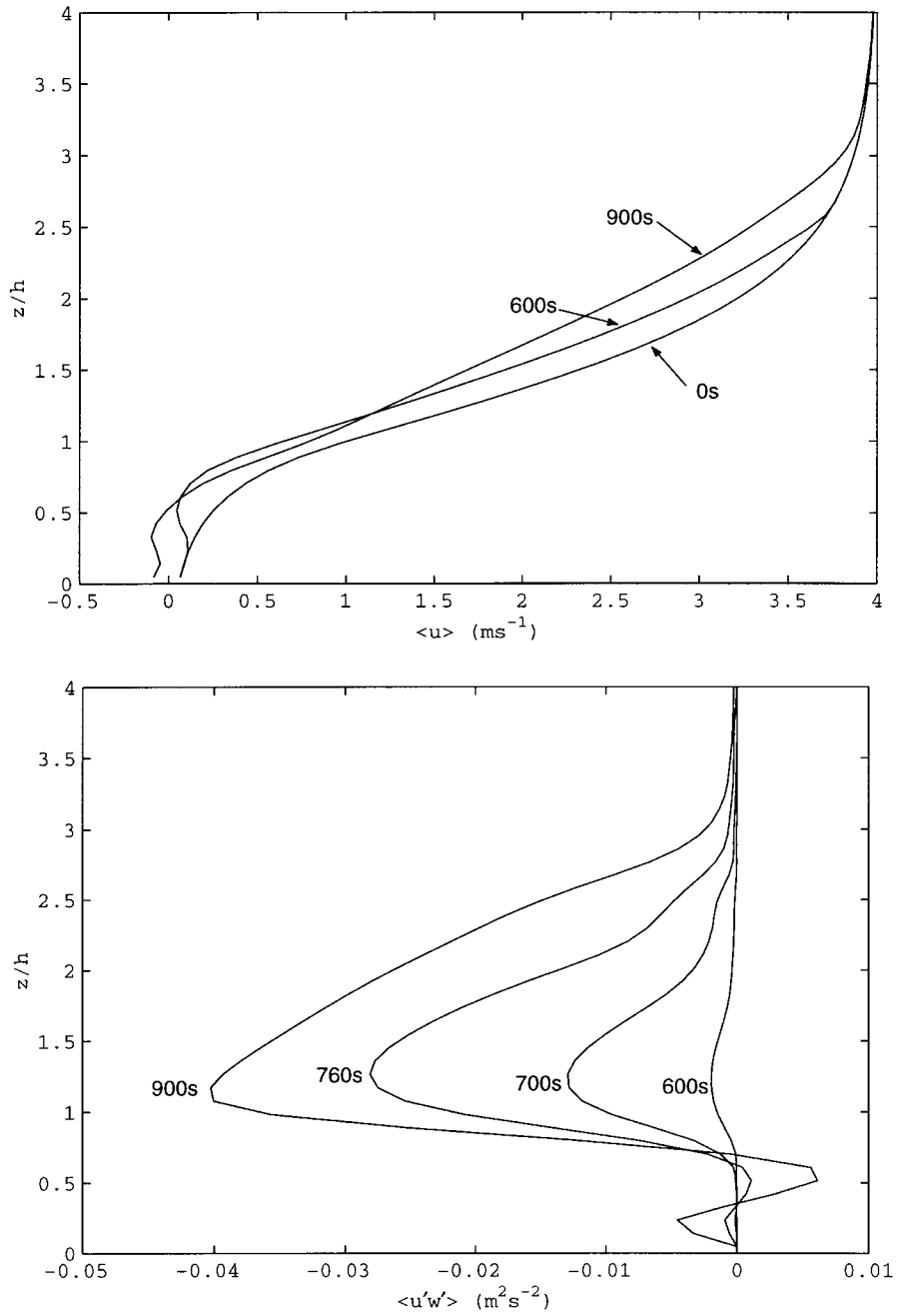

Figure 12. Profiles of horizontal mean wind speed (top) and momentum flux (bottom) at various time steps of model integration.

The lack of a constant flux layer in the presence of wave motion is not a new finding. Divergence/convergence of the momentum flux is predicted by linear theory (e.g., Davis and Peltier, 1977) and was observed in a field experiment (Lee et al., 1997). What impresses us is the rapid increase of momentum flux with time as the wave gains strength. At the wave saturation stage, the momentum flux is two orders of magnitude larger than in the linear growth stage.

Similarly, the wave acts to smooth out the temperature field, with warming below the height of maximum wind shear due to convergence of heat flux and cooling above this height due to divergence of heat flux (Figure 13). Here the heat flux is computed as,

$$\langle w'\theta' \rangle = \frac{1}{L_x} \int_0^{L_x} (w - \langle w \rangle)(\theta - \langle \theta \rangle)\, \mathrm{d}x. \tag{19}$$

The time evolution of the temperature profile bears some resemblance to the observation (Figure 2) in that the vertical gradient in the air layer undergoing vigorous wave motion is substantially reduced. In the wave saturation stage, the original inversion layer is split into two, one in the lower canopy and one above $z/h > 2.5$–3, similar to that reported by Peltier et al. (1976).

Our numerical results and field data show that a canopy wave can significantly modify the mean velocity and temperature fields, even before the wave reaches its finite amplitude. Mixing is accomplished by three mechanisms. First, organized, quasi 2D structures seem to be the dominant form of transport of momentum and heat, especially in the wave core where w' is not in quadrature with either u' or θ' (Figure 10). Second, small-scale eddies play a role at a later stage when overturning structures develop. The overturning first appears at the leading edge of the wave, making the temperature gradient more diffuse than at the trailing edge. Third, mixing also occurs at the time of wave breaking. However, a quantitative assessment of the relative importance of each of these mechanisms requires realistic 3D simulations and is beyond the scope of this study.

5. Conclusions

In this study we propose a four-stage (initiation, growth, saturation, destruction), idealized life cycle for the canopy wave. We conclude that the canopy wave is initiated in an air layer near the treetops. At the height of the wave core center, the velocity fluctuations and temperature time series display the familiar sweep/ejection and inverse ramp patterns, respectively. Further away from this height, w' is in quadrature with u' and T' and the temperature time series become more or less sinusoidal. The height-dependent phase relation is necessary for the wave motion because it allows the wave to extract kinetic energy from the mean flow to support its growth.

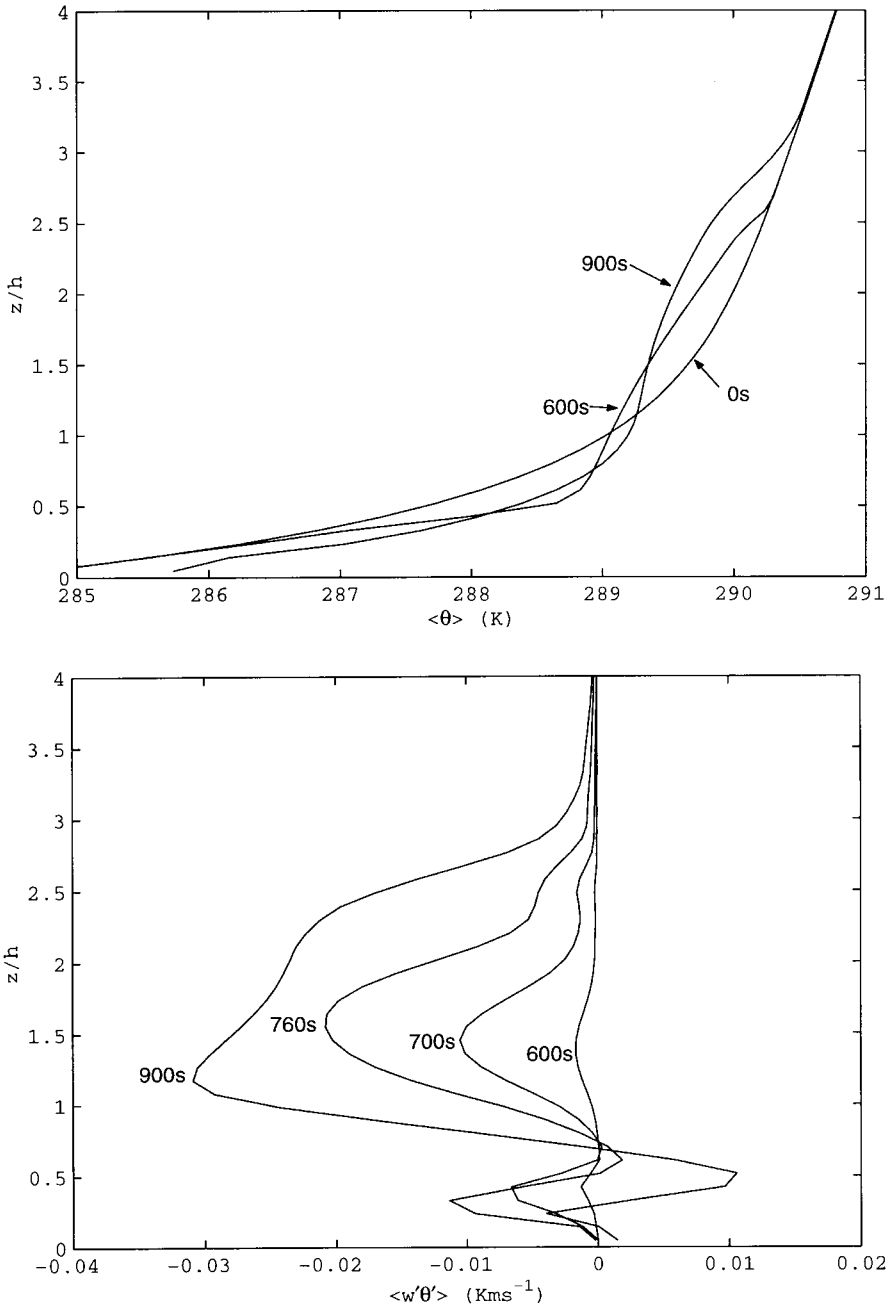

Figure 13. Profiles of horizontal mean temperature (top) and temperature flux (bottom) at various time steps of model integration.

Wave saturation (or finite amplitude wave) is a prominent feature of the field data and is reproduced by our 2D simulations. Distinct isothermal cores are found as a result of wave folding and overturning. The cores travel at a speed that matches the wind speed near the treetops. In this regard, the canopy wave motion differ from propagating buoyancy gravity waves whose phase speed is unrelated to the speed of the medium.

In the wave destruction phase, the leading edge of the wave is destroyed first because this is the place where overturning structures are found (Fig. 4 top panel, Figure 9). The surviving trailing edge exhibits downwind tilting structures, which we believe are essentially the same as the temperature microfronts studied by Gao et al. (1989), Paw U et al. (1992) and others.

Significant modification of the mean velocity and temperature fields is found even before the wave reaches saturation. This is accomplished primarily through mixing caused by the 2D wave motion. The wave motion invalidates the constant-flux-layer assumption made in some field studies of the surface-air exchange. Embedded in the 2D large-scale structures are small-scale overturning features, which also contribute to the mixing especially within the wave core. Further modification of the mean fields occurs when the wave breaks into smaller eddies. Since the background flow is always being modified, the choice of a basic flow for linear stability analysis is not straightforward.

Acknowledgments

This work was supported by the U.S. National Science Foundation through grants ATM-9629497 and ATM-0072864. We thank Dr. D. E. Aylor for his constructive comments on this work. The first author also acknowledges support by a Yale University graduate fellowship, a G. Evelyn Hutchinson fellowship, and a John F. Enders Research Grant.

Appendix A: Algorithm for Computing Phase Speed

Let $\phi_0 = w(x, z, t_0)$ and $\phi_1 = w(x, z, t_0 + \Delta t)$ be the simulated vertical velocity fields at time t_0 and $t_0 + \Delta t$, respectively. The streamwise displacement of the two fields, Δd, is estimated by finding the maximum of the spatial correlation of ϕ_0 and ϕ_1 via an FFT algorithm. The Fourier transformation pairs are denoted as $\phi_0 \Leftrightarrow \Phi_0$ and $\phi_0 \Leftrightarrow \Phi_1$. The correlation theorem states

$$\mathrm{Corr}(\phi_0, \phi_1) \Leftrightarrow \Phi_0 \Phi_1^*,$$

where the asterisk denotes complex conjugate. The (discrete) correlation function is calculated by the inverse FFT transformation according to the correlation theorem. We use sufficiently small Δt so that the primary flow structure does not differ significantly between the two fields.

The estimate of Δd is further improved by a curve fitting routine. Suppose that we have found the discrete maximum of $\mathrm{Corr}(\phi_0, \phi_1)$ at $x' = n\Delta x$, where n is an integer and Δx is the horizontal grid size. We then fit a parabolic curve,

$$C(x) = \alpha(x - x')^2 + \beta(x - x') + \gamma,$$

to the discrete correlation function with a number of points adjacent to x'. The estimate of the displacement is given by

$$\Delta d = x' + \beta/2\alpha,$$

which is more accurate than the original grid size estimate. The phase speed is given by

$$c = \Delta d/\Delta t.$$

References

Almgren, A. S., Bell, J. B., and Szymczak, W. G.: 1996, 'A Numerical Method for the Incompressible Navier–Stokes Equations Based on an Approximate Projection', *SIAM J. Sci. Comput.* **17**, 358–369.

Bergström, H. and Hogström, U: 1989, 'Exchange above a Pine Forest. 2. Organized Structures', *Boundary-Layer Meteorol.* **49**, 231–263.

Davis, P. A. and Peltier, W. R.: 1977, 'Effects of Dissipation on Parallel Shear Instability near the Ground', *J. Atmos. Sci.* **34**, 1868–1884.

Delisi, D. P. and Corcos, G.: 1973, 'A Study of Internal Waves in a Wind Tunnel', *Boundary-Layer Meteorol.* **5**, 121–137.

Drazin, P. G. and Reid, W. H.: 1981, *Hydrodynamic Stability*, Cambridge University Press, London, 527 pp.

Finnigan, J.: 2000, 'Turbulence in Plant Canopies', *Annu. Rev. Fluid Mech.* **32**, 519–571.

Finnigan, J. and Brunet, Y.: 1995, 'Turbulent Airflow in Forests on Flat and Hilly Terrain', in M. P. Coutes and J. Grace (eds.), *Wind and Trees*, Cambridge University Press, pp. 3–40.

Fitzjarrald, D. R. and Moore, K. E.: 1990, 'Mechanisms of Nocturnal Exchange between the Rain Forest and the Atmosphere', *J. Geophys. Res.* **95**, 16,839–16,850.

Gao, W., Shaw, R. H., and Paw U, K. T.: 1989, 'Observation of Organized Structure in Turbulent-Flow within and above a Forest Canopy', *Boundary-Layer Meteorol.* **47**, 349–377.

Hu, X.: 2001, *Nocturnal Wavelike Air Motion in Forests*, Ph.D. Thesis, Yale University, 143 pp.

Klaassen, G. P. and Peltier, W. R.: 1985, 'The Onset of Turbulence in Finite-Amplitude Kelvin–Helmholtz Billows', *J. Fluid Mech.* **155**, 1–35.

Lee, X.: 1997, 'Gravity Waves in a Forest: A Linear Analysis', *J. Atmos. Sci.* **54**, 2574–2585.

Lee, X. and Barr, A. G.: 1998, 'Climatology of Gravity Waves in a Forest', *Quart. J. Roy. Meteorol. Soc.* **124**, 1403–1419.

Lee, X., Neumann, H. H., Den Hartog, G., Fuentes, J. D., Black, T. A., Mickle, R. E., Yang, P. C., and Blanken, P. D.: 1997, 'Observation of Gravity Waves in a Boreal Forest', *Boundary-Layer Meteorol.* **84**, 383–398.

Patnaik, P. C., Sherman, F. S., and Corcos, G. M.: 1976, 'A Numerical Simulation of Kelvin–Helmholtz Waves of Finite Amplitude', *J. Fluid Mech.* **73**, 215–240.

Paw U, K. T., Brunet, Y., Collineau, S., Shaw, R. H., Maitani, T., Qiu, J., and Hipps, L.: 1992, 'On Coherent Structures in Turbulence above and within Agricultural Plant Canopies', *Agric. For. Meteorol.* **61**, 55–68.

Peltier, W. R., Halle, J., and Clark, T. L.: 1978, 'The Evolution of Finite Amplitude Kelvin–Helmholtz Billows', *Geophys. Astrophys. Fluid Dyn.* **10**, 53–87.

Raupach, M. R., Finnigan, J. J., and Brunet, Y.: 1996, 'Coherent Eddies and Turbulence in Vegetation Canopies: The Mixing-Layer Analogy', *Boundary-Layer Meteorol.* **78**, 351–382.

Schilling, V. K. and Janssen, U.: 1992, 'Particle Dispersion due to Dynamical Instabilities in the Lower Stratosphere', *Contrib. Atmos. Phys.* **65**, 259–273.

Shaw, R. H, and Schumann, U.: 1992, 'Large-Eddy Simulation of Turbulent-Flow above and within a Forest', *Boundary-Layer Meteorol.* **61**, 47–64.

Shaw, R. H., den Hartog, G., and Neumann, H. H.: 1988, 'Influence of Foliar Density and Thermal-Stability on Profiles of Reynolds Stress and Turbulence Intensity in a Deciduous Forest', *Boundary-Layer Meteorol.* **45**, 391–409.

Stevens, D. E., Bell, J. B., Almgren, A. S., Beckner, V. E., and Rendleman, C. A.: 2000, 'Small-Scale Processes and Entrainment in a Stratocumulus Marine Boundary Layer', *J. Atmos. Sci.* **57**, 567–581.

Sykes, R. I. and Lewellen, W. S.: 1982, 'A Numerical Study of Breaking Kelvin–Helmholtz Billows Using a Reynolds-Stress Turbulence Closure Model', *J. Atmos. Sci.* **39**, 1506–1520.

Thorpe, S. A.: 1987, 'Transitional Phenomena and the Development of Turbulence in Stratified Fluids: A Review', *J. Geophys. Res.* **92**, 5231–5248.

Werne, J. and Fritts, D. C: 1999, 'Stratified Shear Turbulence: Evolution and Statistics', *Geophys. Res. Lett.* **26**, 439–442.